AFRL-ML-WP-TP-2006-429

A MULTI-SCALE MODELING OF LASER CLADDING PROCESS (PREPRINT)

J. Cao and J. Choi

APRIL 2006

Approved for public release; distribution is unlimited.

**MATERIALS AND MANUFACTURING DIRECTORATE
AIR FORCE RESEARCH LABORATORY
AIR FORCE MATERIEL COMMAND
WRIGHT-PATTERSON AIR FORCE BASE, OH 45433-7750**

NOTICE AND SIGNATURE PAGE

*//Signature//

MARY E. KINSELLA
Processing Section
Metals Branch

//Signature//

JEFFREY R. CALCATERRA, Section Chief
Processing Section
Metals Branch

//Signature//

GERALD J. PETRAK, Asst. Chief
Metals, Ceramics & NDE Division
Materials and Manufacturing Directorate

REPORT DOCUMENTATION PAGE

Form Approved
OMB No. 0704-0188

1. REPORT DATE *(DD-MM-YY)*	2. REPORT TYPE	3. DATES COVERED *(From - To)*
April 2006	Journal Article Preprint	

4. TITLE AND SUBTITLE	5a. CONTRACT NUMBER
A MULTI-SCALE MODELING OF LASER CLADDING PROCESS (PREPRINT)	FA8650-04-C-5704
	5b. GRANT NUMBER
	5c. PROGRAM ELEMENT NUMBER 78011F

6. AUTHOR(S)	5d. PROJECT NUMBER
J. Cao and J. Choi	2510
	5e. TASK NUMBER 00
	5f. WORK UNIT NUMBER 00

7. PERFORMING ORGANIZATION NAME(S) AND ADDRESS(ES)	8. PERFORMING ORGANIZATION REPORT NUMBER
University of Missouri-Rolla B. 37 McNutt Hall 1870 Miner Circle Rolla, MO 65409-0340	

9. SPONSORING/MONITORING AGENCY NAME(S) AND ADDRESS(ES)	10. SPONSORING/MONITORING AGENCY ACRONYM(S)
Materials and Manufacturing Directorate Air Force Research Laboratory Air Force Materiel Command Wright-Patterson AFB, OH 45433-7750	AFRL-ML-WP
	11. SPONSORING/MONITORING AGENCY REPORT NUMBER(S) AFRL-ML-WP-TP-2006-429

12. DISTRIBUTION/AVAILABILITY STATEMENT
Approved for public release; distribution is unlimited.

13. SUPPLEMENTARY NOTES

This paper contains color. PAO Case Number: AFRL/WS 06-0692, 14 Mar 2006.

14. ABSTRACT

Laser cladding is an additive manufacturing process that a laser generates a melt-pool on the substrate material while a second material, as a powder or a wire form, is injected into that melt-pool. Among all laser manufacture processes, laser cladding offers the most extensive variety of possibilities to alter a component at its surface. Despite immense potentials and advancements, the process model of microstructure evolution and its coupling with macro parameter of laser cladding process has not been fully developed. To address this issue, a process model of microstructure evolution has been studied by utilizing a phase-field method. Phase-field method has become a widely used computation tool for the modeling of microstructure evolution with the advantage of avoiding of tracking the interface explicitly and satisfying interfacial boundary conditions. In present work, the numerical solutions of a phase-field model are analyzed. The connection of macro-process and microstructure evolution is examined by considering the relationship of macro- and micro parameters. The effects of thermal noise and melt undercooling on the final microstructure have also been studied. The prediction results are compared with other researchers' results and good agreement was found. Different solidification morphologies of different locations in the melt pool are also investigated. It was found that not the mass transfer but the heat transfer in the melt pool dominates the solidification process.

15. SUBJECT TERMS   laser cladding, additive manufacturing, process model, microstructure evolution

16. SECURITY CLASSIFICATION OF:			17. LIMITATION OF ABSTRACT:	18. NUMBER OF PAGES	19a. NAME OF RESPONSIBLE PERSON (Monitor)
a. REPORT Unclassified	**b. ABSTRACT** Unclassified	**c. THIS PAGE** Unclassified	SAR	46	Mary Kinsella
					19b. TELEPHONE NUMBER *(Include Area Code)* N/A

Standard Form 298 (Rev. 8-98)
Prescribed by ANSI Std. Z39-18

A MULTI-SCALE MODELING OF LASER CLADDING PROCESS

Y. Cao and J. Choi[†]
Department of Mechanical and Aerospace Engineering
University of Missouri – Rolla
Rolla, MO 65409-1060, USA

Abstract

Laser cladding is an additive manufacturing process that a laser generates a melt-pool on the substrate material while a second material, as a powder or a wire form, is injected into that melt-pool. Among all laser manufacture processes, laser cladding offers the most extensive variety of possibilities to alter a component at its surface. Despite immense potentials and advancements, the process model of microstructure evolution and its coupling with macro parameter of laser cladding process has not been fully developed. To address this issue, a process model of microstructure evolution has been studied by utilizing a phase-field method. Phase-field method has become a widely used computation tool for the modeling of microstructure evolution with the advantage of avoiding of tracking the interface explicitly and satisfying interfacial boundary conditions. In present work, the numerical solutions of a phase-field model are analyzed. The connection of macro-process and microstructure evolution is examined by considering the relationship of macro- and micro parameters. The effects of thermal noise and melt undercooling on the final microstructure have also been studied. The prediction results are compared with other researchers' results and good agreement was found. Different solidification morphologies of different locations in the melt pool are also investigated. It was found that not the mass transfer but the heat transfer in the melt pool dominates the solidification process.

[†] Corresponding author: J. Choi, jchoi@umr.edu(e-mail), 573-341-6560(O)

PREPRINT

I. Introduction

Laser cladding is an additive manufacturing process that a laser generates a melt-pool on the substrate material while a second material, as a powder or a wire form, is injected into that melt-pool. The cladding alloy can form a strong bond to the substrate, with a minimum melting of the substrate. Among all laser processes, laser cladding offers the most extensive variety of possibilities to alter a component at its surface. For example it can be used for protection of materials against the wear, corrosion and oxidation, and for the refurbishing a high cost industrial product by using a coating with improved properties.

During the laser cladding process, several complex phenomena occur as the laser interacts with both incoming material and the substrate material. These phenomena include thermal transport, fluid flow, mass transport and solidification, and so on. Heat and fluid flow have been studied numerically and experimentally by other researchers [1,2]. There are many researchers who observed the microstructure evolution of the laser cladding process by using optical, SEM, TEM technique [25-27], however, the modeling of microstructure evolution of the solidification process during the laser cladding has not been fully developed and studied.

Phase-field method has recently become a widely used technique to model the formation of complex interfacial patterns in solidification process. It has been the main topic of recent review literatures [4-5, 28]. With this model, one can significantly enhance our theoretical understanding of the solidification process, especially the microstructure evolution in the metals, including pure substances and alloys. In the phase-field model, the interface between the solid and liquid is considered as a diffuse interface instead of a sharp interface. The phase field

variable ϕ is introduced to indicate the state of the phase. The quantity ϕ is a continuous variable that takes a constant value in the bulk phases, i.e., -1 for liquid and 1 for solid, and changes from -1 to 1 steeply through the interface. The evolution of ϕ is governed by a phase-field equation, which is coupled with thermal diffusion equation and composition equation in the phase-field model to describe the transport phenomena in the solidification process. The most valuable property of the phase-field model is the fact that there is no need to explicitly track the interface or even provide interfacial boundary conditions [6]. So it is easy to implement numerically compared with other interface front tracking method.

Wheeler, Boettinger and McFadden developed the so-called WBM phase-field model to deal with alloy solidification [7,8]. This model was derived in a thermodynamically consistent way and used to study the solute trapping of the isothermal binary alloy in rapid solidification [9]. It was shown that the solute trapping occurs when the solute diffusion length is comparable to the diffuse interface thickness. This model has been widely used in many applications, including dendrite growth, solute trapping, eutectic solidification, sidearm branching, etc [4]. Kim *et al.* [10] proposed another phase-field model by using a different definition of the free energy. This model was used to study the binary alloy solidification and dendrite growth. Their results are in good agreement with the experimental observations. Wheeler *et al.* [7] have shown that the interface thickness must be smaller than the capillary length for the solution to converge to the sharp-interface limit. Karma and Rappel [11] reconsidered this issue and proposed a thin interface analysis. They found that the interface thickness only needs to be small compared to the "mesoscale" of the heat and/or solute diffusion field. Their asymptotic analysis greatly enhanced the computational efficiency of the phase-field simulation and they made the first time fully

resolved computations for three-dimensional dendritic growth [12, 13]. Beckermann *et al.* [6, 14, 15] further conducted much effective work in this area. They presented a simpler derivation of the phase-field equation starting from the classical velocity-dependent Gibbs-Thomson interface condition. They also studied the pure metal dendritic growth, binary alloy solidification coupled with heat and solute diffusion, and the solidification phenomena with fluid flow [15].

Very few models for microstructure evolution of laser cladding process have been reported [3, 24], and almost all the above models [6-15] were used to deal with the ideal process (pure metal, isothermal binary alloy, etc). In this paper a two-dimensional phase-field model based on Karma and Beckermann's analysis [13, 14] was developed to explore the microstructure evolution in a real physical process, laser cladding. Anisotropy effect was included in this model, while the interface kinetics was neglected by properly choosing the calculation parameters. This phase-field model was coupled with the macro-process model and served as micro-scale model to simulate the laser cladding process.

This paper is structured as following: The macro-scale model of laser cladding process is presented firstly. This model is used to get the macro-temperature field and other related physical parameters, and followed by the phase-field model. The linking between the macro-scale model and phase-field model is carried out, considering the relationship of the macro- and micro-scale process parameters. The phase-field model is validated, comparing the interface shape and dendrite tip velocity with other researchers' results for pure metal dendrite growth. Next, a typical two-dimensional binary alloy dendrite growth is presented for the case of coupled heat and solute diffusion. Then, the effects of thermal noise and melt undercooling on the final

microstructure have been studied. Different solidification morphologies of different locations in the melt pool are also investigated.

II. Macro-scale Model

The macro-scale model was used in this study to get the macro-scale temperature field, which will be used in the phase-field calculation. The transport phenomena of melt pool were studied, including the melt pool shape and size, and so on. Most work of this part is based on the previous study of the author's research group [16].

The basic assumptions of this model are as follows:

1. A laser beam having a defined power distribution strikes the surface of an opaque material of finite depth, and length.

2. Only part of the energy is absorbed by the workpiece and powder. Studies show that the amount of laser energy absorbed by the different materials is 37%-60% [17, 23].

3. The absorbed energy induces surface tension driven flow due to the high-temperature gradient.

4. The liquid metal is Newtonian, so the Navier-Stokes equation is applicable.

5. All properties of the liquid and solid metal are constant, independent of temperature. (This allows simplifications of the model; however, variable properties can be treated with slight modifications.)

A. Governing Equations

The continuity equation, momentum equation and energy equations based on continuum formulation are modified and used in the present study. They are given below:

Continuity equation:

$$\frac{\partial}{\partial t}(\rho) + \nabla \cdot (\rho V) = 0 \tag{1}$$

Momentum equation:

$$\frac{\partial}{\partial t}(\rho u) + \nabla \cdot (\rho V u) = \nabla \cdot (\mu_l \frac{\rho}{\rho_l} \nabla u) - \frac{\partial p}{\partial x} - \frac{\mu_l}{K} \frac{\rho}{\rho_l}(u - u_s) \tag{2}$$

$$\frac{\partial}{\partial t}(\rho v) + \nabla \cdot (\rho V v) = \nabla \cdot (\mu_l \frac{\rho}{\rho_l} \nabla v) - \frac{\partial p}{\partial y} - \frac{\mu_l}{K} \frac{\rho}{\rho_l}(v - v_s) + \rho.g \tag{3}$$

Energy equation:

$$\frac{\partial(\rho h)}{\partial t} + \nabla \cdot (\rho V h) = \nabla \cdot (k_t \nabla T) - \nabla \cdot (\rho(h_l - h)(V - V_S)) \tag{4}$$

Evolution of free surface:

$$\frac{\partial F}{\partial t} + (V \cdot \nabla)F = 0 \tag{5}$$

Note that the momentum and energy equations contain the phase interaction terms. In the equations (1)-(4), the subscript l and s denote the liquid and solid, respectively. The density ρ, thermal conductivity k_t are defined as the average value of liquid and solid state based on the solid volume fraction g_s and liquid volume fraction g_l. The specific heat c_p, velocity V and the enthalpy h are defined as the average value of liquid and solid state based on the solid mass fraction f_s and liquid mass fraction f_l. u and v are the X, Y components of velocity. u_s and v_s are the tangential and normal velocity components at the free surface. K is the permeability of the two-phase mushy region which is modeled as a porous media. μ_l is the dynamic viscosity.

In equation (5), F expresses the fractional volume occupied by fluid in that computational cell. *F* takes a value of unity at a cell in space occupied by fluid and a value of zero if fluid does not

occupy that cell, and cells with F value between zero and unity are partially filled with fluid and identified as surface cells. The liquid-vapor interface is located at the $F = 0.5$ contour.

B. Boundary Conditions

With the liquid-vapor free surface, the shear stress and normal stress balance is considered to get the boundary condition of the velocity at the free surface. The energy balance included the effect of laser heating, and heat loss from convection, radiation and evaporation. With other boundary surfaces, the velocity is considered as zero and energy balance considered the heat loss from convection and radiation. Details of the formulations for the boundary conditions can be found in the reference [16].

III. Phase-field Model

One macro-cell adjacent to solid-liquid interface will be chosen to carry out the microstructure evolution calculation. Thus the whole calculation domain will be this macro-cell. The behavior of phase field variable in this domain is governed by the phase-field equation, which is coupled with equations for heat and solute diffusion. The interface between liquid and solid is represented by smooth but rapid change of the phase-field variable. Following assumptions were made for the phase-field model.

1. Influence of fluid flow is not considered in the phase-field model. Only a very tiny macro-cell is picked up to carry out the micro-phase-field calculation since the effect of fluid flow is not very significant.

2. The thermo-physical properties such as thermal conductivity, specific heat, density, and so on are assumed constant and equal in liquid and solid state.

7

3. Considering the solute diffusivity in solid state is very small compared with that in liquid state, the solute diffusion in solid state is neglected.

4. The interface kinetics effect is neglected.

5. For the sake of simplicity, the partition coefficient of the solidification process is assumed to be same as the one in the equilibrium state.

A. Governing Equations

To compare the result with other researchers', the dimensionless temperature and composition are employed as following:

$$\theta = \frac{T - T_m - mc_\infty}{L/c_p} \tag{6}$$

$$\chi = \frac{c - c_\infty}{(1-k)c_\infty} \tag{7}$$

where T_m is the melting temperature of pure solvent, m is the liquidus line slope of the alloy phase diagram, c_∞ is the value of composition, c, far from the interface, which equals the initial composition of the alloy, L is latent heat of melting, k is the equilibrium partition coefficient. Additionally, the following dimensionless variables are defined;

$$u = \ln\left[\frac{2c/c_\infty}{1 + k - (1-k)\phi}\right] \tag{8}$$

and

$$U = \frac{e^u - 1}{1 - k} \tag{9}$$

where u is a dimensionless measure of the deviation of the chemical potential from its equilibrium value at a reference temperature, and U is used to change the variable of the composition equation and considered as the dimensionless composition.

The phase-field equation, composition equation and energy equation are obtained in terms of the dimensionless temperature and composition as follows:

$$\tau \frac{\partial \phi}{\partial t} = W^2 \nabla^2 \phi + \phi - \phi^3 - (1 - \phi^2)^2 \lambda (\theta + Mc_\infty U) \tag{10}$$

$$\frac{1+k}{2} \frac{\partial U}{\partial t} = \frac{1}{2} \frac{\partial}{\partial t} \left\{ \phi [1+(1-k)U] \right\} + \nabla \cdot \left\{ D \frac{1-\phi}{2} \nabla U + \frac{W}{2\sqrt{2}} [1+(1-k)U] \frac{\partial \phi}{\partial t} \frac{\nabla \phi}{|\nabla \phi|} \right\} \tag{11}$$

$$\frac{\partial \theta}{\partial t} = \alpha \nabla^2 \theta + \frac{1}{2} \frac{\partial \phi}{\partial t} \tag{12}$$

where τ is the relaxation time in phase-field model, W is the interface thickness, λ is a dimensionless parameter which controls the strength of the coupling between the phase and thermal/solutal diffusion fields, and D is the solutal diffusivity in the liquid, M is the scaled liquidus slope which is defined as;

$$M = \frac{-m(1-k)}{L/c_p} \tag{13}$$

To eliminate the interface kinetics, τ is chosen to be a function of U in the phase-field model, which is defined by

$$\tau = \tau_0 \left\{ \frac{D}{\alpha} + Mc_\infty [1+(1-k)U] \right\} \tag{14}$$

where τ_0 is the measure scale of time in current study.

B. Anisotropy Effect

To include anisotropy effect, we choose a standard fourfold anisotropy defined by

$$W(n) = W_0 a_s(n) \qquad \tau(n) = \tau_0 a_s^2(n) \qquad (15)$$

$$a_s(n) = 1 - 3\varepsilon_4 + 4\varepsilon_4 \frac{(\partial\phi/\partial x)^4 + (\partial\phi/\partial y)^4}{|\nabla\phi|^4} \qquad (16)$$

Combining equations (14) – (16), we can obtain that

$$\tau = \tau_0 a_s^2(n)\{\frac{D}{\alpha} + Mc_\infty[1 + (1-k)U]\} \qquad (17)$$

In this manner, the anisotropy effect can be incorporated and the interface kinetics be eliminated at the same time.

C. Boundary Conditions

The temperature boundary condition can be found from the macro-neighbor cells of the selected cell. In the present study, the Dirichlet boundary condition is used in the phase-field calculation. Because it is assumed there is no fluid flow in the selected cell previously, there is also no mass flow between the whole calculation domain and neighbor cells. The Dirichlet boundary condition is also applied for composition field.

To the phase-field variable, a zero-Newmann condition is employed to describe the boundary of the calculation domain.

IV. Numerical Method

In the present study, the macro-model was employed to calculate the temperature, fluid pressure and velocity fields of the whole calculation domain. Each macro-cell has four state variables: temperature, pressure, velocity and fractional volume (F). One macro-cell near the solid-liquid

10

interface is chosen to carry out for the micro-scale calculation in order to simulate the evolution of solidification microstructure. This macro-cell is re-meshed making much finer micro-cells. Each micro-cell has three state variables: temperature, phase field and concentration. In the temporal domain, there are two time steps: Δt for macro-calculation and much smaller δt for phase-field calculation. Each Δt is again divided into 5 small micro-time steps in current calculation. This macro- and micro-scale coupling scheme is shown in Fig. 1.

To couple the two different scale calculations, the temperature of the neighbor cells of the micro-calculation domain is applied as the temperature boundary condition. In each macro-time step, this boundary temperature is considered as constant. At the next macro-time step, this boundary temperature will be changed to another value, which is determined by the macro-scale model.

A semi-implicit SOLA-VOF [18] based algorithm was used for the solution of continuity and momentum equations (1)-(3) in the macro-scale model. The thermal energy transport equation (4) was solved using an explicit finite volume approximation. A fixed-grid system of 200 x 100 uniform grid points was utilized for the cladding domain of 4 mm x 2 mm. Each grid has a cell size of 20 μm x 20 μm. An explicit finite difference scheme was used to solve the phase-field equation, composition equation, and energy equation, described in the Equations (10)-(12) in micro-scale model. The grid numbers used in this study are either1000 x 1000 or 1500 x 1500 in different cases.

It is assumed that the nucleation begins at a certain undercooling. Initially, the micro-calculation domain is filled with an amount of supercooled melt. Once the undercooling reaches the given

value, then, the nucleation will take place instantly and a solid seed will be present in the center of the calculation domain, followed by that the growth process of the solid seed will be controlled by phase-field model and appropriate boundary conditions.

A. Iteration Procedures

The steps of iteration procedure for the macro-scale calculation are as following:

(1) Initialize the velocities, pressure, temperature and VOF function.

(2) Solve the momentum equations utilizing a two-step projection method. Surface tensions are solved and included into momentum equations as body forces. In this step, new velocities and pressure are solved.

(3) Advance VOF function in time domain to update new free surface.

(4) Solve the energy equation using new velocities obtained in step 2.

(5) Check the undercooling. If it reaches the given value, the phase-field calculation will begin. If not, go to step 6.

(6) Update old velocities, pressure, temperature and VOF function using new values, and back to step 2 for next iteration until the time to finish calculation is reached.

The iteration procedures for micro-calculation are as following:

(1) Initialize the temperature, composition and phase field variable.

(2) Solve the phase-field equation utilizing an explicit finite difference method.

(3) Solve the composition equation using new phase-field variables obtained in step 2.

(4) Solve the energy equation using new phase-field variables obtained in step 2.

(5) Update old temperature, concentration and phase field variable using new values, and back to step 2 for next iteration until the phase-field or composition field reach the boundary of calculation domain.

B. Numerical Stability

With the macro-scale calculation, the numerical difference equations are subjected to linear numerical stability conditions that are detailed in [19].

To the phase-field model, the time step is

$$\delta t = \frac{1}{4}\min(\delta t_1, \delta t_2) \tag{18}$$

where

$$\delta t_1 = \frac{1}{2\alpha}(\Delta x^2 + \Delta y^2) \quad \delta t_2 = \frac{\tau_0 \Delta x^2}{W_0^2} \tag{19}$$

δt_1 is derived from thermal energy equation and δt_2 from phase-field equation. It is difficult to determine the stable time step for composition equation. But from numerical test, it is found that the time step determined by equation (18) can keep the composition calculation stable.

V. Simulation Results and Discussion

The results of different cases are presented in this section. First, the macro-scale process was simulated using the macro-scale model developed above. To validate the current micro-scale model, a pure metal solidification case was calculated and compared with Karma's result [13]. A binary alloy dendrite growth was also simulated. Finally, three coupling cases were calculated

with different locations in the melt pool. Simulations of all the cases are based on the material

properties of H13 tool steel and process parameters shown in Table 1. To make the calculation

simple, the material used in this study was assumed as a binary alloy.

A. Results by Macro-scale Model

To carry out the phase-field calculation, the macro-scale model was used first to calculate the

whole domain temperature field. Several snap shots of the calculation results are shown in Fig. 2.

Fig. 2(a) shows the temperature field at the simulation time 32 ms, and every 2 ms until 38 ms,

as shown in Fig. 2(b)-(d). Fig. 2 also shows the powder injection process. From Fig. 2(a) to (d),

it can be seen clearly the first powder, appeared in Fig. 2(a), falls into the melt pool as shown in

Fig. 2(d). It is also observed that the deeper the droplet is approaching into the melt pool and

pushing the fluid away, the higher the speed of the flow is at the top surface.

B. Pure Metal Dendrite Growth

To validate the current phase-field model, a pure metal solidification case was calculated. In

pure metal case, only phase-field equation and thermal equation need to be solved. And the Mc_∞

term in the phase-field equation should be zero in this pure metal solidification case. The

dimensionless undercooling threshold value is 0.55 in present study. According to Karma [13],

the length of solidification microstructure is scaled by W_0, and the time by τ_0. Setting $W_0 = 1$, τ_0

= 1, other parameters used in this pure metal calculations are as following: $\lambda = 6.3829$, $\alpha = 4$, Δx

= $\Delta y = 0.4$, $\delta t = 0.008$, $\varepsilon_4 = 0.05$. The grid number is 1000x1000. Only the first quarter of

calculation domain was calculated considering the symmetry. For the comparison with Karma's

results, the interface shape is calculated, as shown in Fig. 3, and the interface position is chosen

at the $\phi = 0$ contour, which was simulated in every 5000-iterations. It is evident that this interface shape is almost identical to that by Karma's [13], which is considered that this model is qualitatively correct.

The dendrite tip velocity was also calculated in this pure metal case according to the following equation:

$$V_{tip} = \frac{\partial \phi / \partial t}{|\nabla \phi|} \tag{20}$$

The dimensionless dendrite tip velocity is calculated based on the following equation:

$$\overline{V}_{tip} = \frac{V_{tip} d_0}{\alpha} \tag{21}$$

where d_0 is the capillary length. According to Karma's result [13], the steady state dimensionless dendrite tip velocity is 0.0170. In our current model, the converged dendrite tip velocity, as shown in Fig. 4, is 0.0164, which is pretty close to Karma's result. It appears that this model is quantitatively correct and the difference is about 3.5%.

C. Binary Alloy Solidification

In order to compare our calculation with comparable results available in the literature [14], it is suitable to define similar parameters. Thus, the Lewis number (Le), which is defined as the ratio of thermal diffusivity α to solute diffusivity D, is chosen and used for this comparison. Based on the validation of pure metal solidification, dendrite growth for a binary alloy case was simulated. The simulation parameters are chosen as following: $MC_\infty = 0.1$, k = 0.15, Le = 20, D = 4.0, $\delta t = 0.0004$. Other parameters were kept as same as pure metal dendrite growth case. Fig. 5 shows

15

the calculation results of the phase field (ϕ), dimensionless composition field (U), and dimensionless temperature field (θ) at dimensionless time 52 (i.e. the iteration number, as $\delta t = 0.0004$ and $\tau_0=1$, is 52/0.0004=130000) in current model. The final solid/liquid composition can be calculated with Equations (8) and (9). Comparing Fig. 5(b) with 5(c), it appears that the thermal boundary layer thickness is much larger than that of the solutal boundary layer. This arises from the fact that the thermal diffusivity is 20 times larger than the solutal diffusivity. The results of current model were compared with Ramirez's [14]. Excellent agreement was also found except the range of composition field. It was explained that different value of Lewis number was used in the calculation, which is Le=20 in current model, whilst Le=40 in Ramirez's calculation.

D. Results for Coupling Cases

Three different coupling cases based on the location in the melt pool were investigated in this study. The cell location is shown in Fig. 6. All other simulation parameters were kept same in these three cases.

Case 1: The macro cell was chosen from cell location 1 in Fig. 6, which is located on the solid/liquid interface and on the left of melt pool. Considering the workpiece move direction (to the left), one can figure out that there will be certain incoming heat transfer from right to left during the following time step. This can be shown clearly from the dimensionless temperature evolution of Fig. 7. Fig. 7 also shows the microstructure and composition evolution of cell location 1 from dimensionless time, 10 to 60. An interesting observation is that the left dendrite

tip shows a greater growth velocity than the right one with the incoming heat flux from right to left side.

Case 2: The macro cell was picked up from the left bottom corner of the melt pool, which is cell location 2 in Fig. 6. The microstructure, dimensionless temperature and composition evolution were shown in Fig. 8. It can be found that the heat flux direction in Fig. 8 is along the diagonal of the calculation domain, from the right top corner to the left bottom corner, and that the left and bottom dendrite tips grow faster than the right and top ones.

Case 3: The macro cell was selected from the cell location 3 shown in Fig. 6. This cell locates in the right front of the melt pool, which will soon be heated by the external energy source (laser in this study). Fig. 9 shows the corresponding evolution of microstructure, dimensionless temperature and composition. The initial seed in the calculation domain undergoes a growth in the first two frames and subsequently melt in the remaining frames. The interesting point is that the faster growth direction in the first two frames is identical to the heat flux direction, which is from left top corner to the right bottom corner.

Based on the observation of the above three cases which share same calculation parameters except the location in the melt pool, one can reach the conclusion that it was the heat transfer, not the mass transfer, that dominates dendrite growth pattern in the binary alloy solidification microstructure during laser cladding process.

E. Effect of Thermal Noise

It was reported that the conserved noise in heat current is the most dominant one according to

Karma's study on dendritic sidebranching with thermal noise [20]. In the present study, a

different method [21] is employed to include the thermal noise effect. To simplify the

calculation, only the pure metal case was calculated in this section. The thermal energy equation

with thermal noise changes to

$$\frac{\partial \theta}{\partial t} = \alpha \nabla^2 \theta + \frac{\partial \phi}{\partial t} + S\xi(1+\phi)(1-\phi) \tag{22}$$

where S is the thermal noise strength, ξ is a random number from -1 to 1. The thermal noise

term in Equation (22) shows that the thermal noise will be vanished at the bulk state (solid or

liquid) and only valid at the diffuse interface region. It is obvious that the highest thermal noise

is present if the ϕ equals to 0, where the solid/liquid interface is defined in this work.

Fig. 10 shows the effect of thermal noise on the dendrite growth pattern, varying thermal noise

strength. When the thermal noise strength is small (S = 4), only very small variation of the

growth pattern can be observed along the dendrite. With the increase of the strength, the

variation becomes larger and easier to observe. It can be observed that different dendritic

sidebranching, showing secondary arm, even the tertiary arm, appears in the growth pattern.

Also, it is observed that the asymmetry effects, which arise from the random number (ξ) in the

thermal noise term, can be present in the final microstructure. When the thermal noise strength

is much higher, i.e., S = 25, as shown in Fig. 10 (e), the bifurcation phenomenon appear in one of

the primary dendrite arm. The detailed mechanism of this phenomenon is beyond of this study

and still investigating, thus will not be discussed further.

18

F. Effect of Undercooling

The effect of undercooling on the dendrite growth pattern of the solidification microstructure was also investigated. In this study, all other parameters were kept same with the pure metal case, and only the threshold undercooling was varied from 0.45 to 0.75.

Fig. 11 shows the calculated phase field with different undercooling. It is clear that one can get sharp and smooth dendrite shape if we choose $\Delta = 0.55$. If the undercooling is smaller than the value, as shown in Fig.11 (a), the primary dendrite arm will become coarser. Meanwhile, if the undercooling is greater than 0.55, as shown in Fig. 11 (b), there will be some bifurcation in the final phase field. Increasing the undercooling much higher, as shown in Fig. 11 (c), much more bifurcation will be appeared. It appears that the dendrite growth pattern varies from dendrite to globular as the undercooling increases. It also turned out that the CPU time for the simulation is decreasing dramatically with the increase of the undercooling. Considering the same domain size, it is evident that the dendrite tip velocity increases dramatically with the increase of the undercooling. This phenomenon was also reported by Zhao et al. [22], and according to their analysis the dendrite tip velocity is proportional to Δ^2 in 2D case with small Peclet number.

VI. Concluding Remarks

1. A multi-scale model for laser cladding process has been developed by coupling the macro-scale model based on VOF formulation with micro-scale model based on phase-field model. In phase-field model, the effect of anisotropy was included in predicting dendrite growth pattern but the interface kinetics was neglected to simplify the modeling work. This multi-scale model can be used to effectively simulate solidification microstructure during laser cladding process.

19

2. To verify the micro-scale model based on phase-field approach, pure metal dendrite growth was investigated. A good agreement was found with the results reported in literature. Dendritic growth for the binary alloy was also simulated, and the temperature and composition distribution in the dendritic growth showed similar patterns observed by other researchers.

3. Phase-field, dimensionless temperature and composition at different cell locations in the melt pool during the laser cladding were investigated linking macro-scale model with micro-scale model. It was found that the heat transfer, not mass transfer, dominates dendrite growth pattern of solidification microstructure for the binary alloy case.

4. The effects of thermal noise and undercooling on the growth pattern of solidification microstructure were also studied. It was found that some secondary arm or even tertiary arm in the dendrite growth process could be side-branched if appropriate thermal noise strength was chosen. Also, if the undercooling was chosen appropriately, smooth dendrite pattern with suitable dendrite tip velocity could be obtained.

References

[1] Hoadley, A.F.A., Rappaz, M. (1992) A thermal model of laser cladding by powder injection, Metall. Trans. 23B, 631-643.

[2] Picasso, M., Marsden, C., Wagnieres, J.-D., Frenk, A., Rappaz, M. (1994) A simple but realistic model for the laser cladding process, Metall. Trans. 25B, 281-291.

[3] Kar, A. and Mazumder, J. (1989) Extended solid solution and nonequilibrium phase diagram for Ni-Al alloy formed during laser cladding, Metall. Trans. 20A, 363-371.

[4] Boettinger, W.J., Warren, J.A., Beckermann, C. and Karma, A. (2002) Phase-field simulation of solidification, Annual Review of Materials Research 32, 163-194.

[5] Chen, Long-Qing (2002) Phase-field models for microstructure evolution, Annual Review of Materials Research 32, 113-140.

[6] Beckermann, C., Diepers, H.-J., Steinbach, I., Karma, A., and Tong, X. (1999) Modeling melt convection in phase-field simulation of solidification, Journal of Computational Physics 154, 468-496.

[7] Wheeler, A.A., Boettinger, W.J., and McFadden, G.B. (1992) Phase-field model for isothermal phase transitions in binary alloys, Physical Review A 45, 7424-7440.

[8] Wheeler, A.A., Boettinger, W.J., and McFadden, G.B. (1993) Phase-field model of solute trapping during solidification, Physical Review E 47, 1893-1909.

[9] Ahmad, N.A., Wheeler, A.A., Boettinger, W.J., and McFadden, G.B. (1998) Solute trapping and solute drag in a phase-field model of rapid solidification, Physical Review E 58, 3436-3450.

[10] Kim, S.G., Kim, W.T., and Suzuki, T. (1999) Phase-field model for binary alloys, Physical Review E 60, 7186-7197.

[11] Karma, A., and Rappel, W.–J. (1996) Phase-field method for computationally efficient modelling of solidification with arbitrary interface kinetics, Physical Review E 53, 3017-3020.

[12] Karma, A., and Rappel, W.–J. (1996) Numerical simulation of three-dimensional dendritic growth, Physical Review Letters 77, 4050-4053.

[13] Karma, A., and Rappel, W.–J. (1998) Quantitative phase-field modelling of dendritic growth in two and three dimensions, Physical Review E 57, 4323-4349.

[14] Ramirez, J.C., Beckermann, C., Karma, A., and Diepers, H.–J (2004) Phase-field modeling of binary alloy solidification with coupled heat and solute diffusion, Physical Review E 69, 051607.

[15] Tong, X., Beckermann, C., Karma, A. and Li, Q. (2001) Phase-field simulations of dendritic crystal growth in a forced flow, Physical Review E 63, 061601.

[16] Choi, J., Han, L., Hua, Y. (2005) Modeling and experiments of laser cladding with droplet injection, ASME Journal of Heat Transfer, **127**, pp. 978-986.

[17] Li, L.J., and Mazumder, J. (1985), in Proceedings of Laser Processing of Materials, Metallurgical Society of American Institute of Metallurgical Engineers, Warrendale, PA, 35-50.

[18] Nichols, B.D., Hirt, C.W., and Hotchkiss, R.S. (1980) SOLA-VOF: a solution algorithm for transient fluid flow with multiple free boundaries, LA-8355, Los Alamos National Laboratory.

[19] Hirt, C.W., and Nichols, B.D. (1981) Volume of fluid (VOF) method for the dynamics of free boundaries, Journal of Computational Physics 39, 201-225.

[20] Karma, A., and Rappel, W.–J. (1999) Phase-field model of dendritic sidebranching with thermal noise, Physical Review E 60, 3614-3625.

[21] Li, X., Guo, J., Su, Y., Jia, J. and Fu, H. (2004) Research of the equiaxed dendritic growth in the undercooled melt of the pure metal by phase-field method, ACTA Metallurgica Sinica 40 (1), 31-35 (in Chinese)

[22] Zhao, D., Tao, J. and Liu, B. (2003) Influence of phase-field parameters on the dendrite morphology, ACTA Metallurgica Sinica 39 (8), 813-816 (in Chinese)

[23] Gedda, E., Powel, J., Wahlstöm, G., Li, W.-B., Engström, H, and Magnusson, C. (2002) Energy Redistribution during CO_2 Laser Cladding, Journal of Laser Applications, 14(2), 78-82.

[24] Hung, C-F, and Lin, J. (2004) Solidification Model of Laser Cladding with Wire Feeding Technique, Journal of Laser Applications, 16(3), 140-146.

[25] Zhong, M.L, Yao, K.F., Liu, W.J., Goussain, J.C., Mayer, C., and Becker, A. (2001) High-power laser cladding Stellite 6+WC with various volume rates, Journal of Laser Applications, 13(6), 247-251.

[26] Choi, J., Choudhuri, S.K., and Mazumder, J. (2000) Role of Preheating and Specific Energy Input on the Evolution of Microstructure and Wear Properties of Laser Clad Fe-Cr-C-W Alloys, J. of Materials Science, 35(13), 3213-3219.

[27] Sircar, S., Chattopadhyay, K., and Mazumder, J. (1992) Nonequilibrium Synthesis of $NbAl_3$ and Nb-Al-V Alloys by Laser Cladding. 1. Microstructure Evolution, Metal. Trans. A, 23(9), 2419-2429.

[28] Sekerka, R.F. (2004) Morphology: from Sharp Interface to Phase Field Models, J. of Crystal Growth, 264, 530-540.

NOMENCLATURE

$a_s(n)$	anisotropy
c	composition of material
C_{pl}	specific heat of liquid
C_{ps}	specific heat of solid
c_∞	composition far from the interface
d_0	capillary length
D	solutal diffusivity
F	volume of fluid function
f_l	liquid mass fraction
f_s	solid mass fraction
g_l	liquid volume fraction
g_s	solid volume fraction
h	enthalpy
h_l	liquid enthalpy
h_s	solid enthalpy
I	grid number in x direction
J	grid number in y direction
k	equilibrium partition coefficient
k_t	thermal conductivity
K	permeability of the two-phase mushy region
L	latent heat of melting
L_e	Lewis number
L_m	latent heat of fusion of material
L_v	latent heat for liquid-vapor phase change
m	slope of liquidus line
M	scaled liquidus slope
p	pressure
S	thermal noise strength
T	temperature
T_l	liquidus temperature
T_m	melting temperature of pure solvent
T_s	solidus temperature
t	time
Δt	macro-time step
δt	micro-time step
U	dimensionless measure of composition
u	velocity in X-direction
v	velocity in Y-direction
u_s	tangential velocity at free surface
v_s	normal velocity at free surface
V	velocity vector
V_{tip}	dendrite tip velocity

$\overline{V}_{tip}$	dimensionless dendrite tip velocity
w	interface thickness
W_0	length scale in current study
Δ	undercooling
Δx	mesh spacing along X axis
Δy	mesh spacing along Y axis
Subscript	
l	liquid phase
s	solid phase
Greek symbols	
α	thermal diffusivity
χ	dimensionless composition
ε_4	anisotropy coefficient
ϕ	phase-field
μ_l	dynamic viscosity of liquid metal
λ	strength of coupling between phase and diffusion fields
θ	dimensionless temperature
ρ	density
ρ_l	density of liquid
ρ_s	density of solid
τ	relaxation time in phase-field model
τ_0	time scale in current study
ξ	Random number between -1 and 1

Table Captions

Table 1. Material properties and process parameters

Table 1. Material properties and process parameters

Property	Symbol	Value
Powder absorptivity	α	0.35
Power absorptivity	β	0.3
Specific heat of liquid	c_{pl}	800 J/(kgK)
Specific heat of solid	c_{ps}	700 J/(kgK)
Diameter of powder	D	100 μm
Conductivity of liquid	k_l	21 W/(mK)
Conductivity of solid	k_s	21 W/(mK)
Latent heat of melt	L_m	2.7×10^5 J/kg
Latent heat of evaporation	L_v	6.34×10^6 J/kg
Powder mass rate	m_p	5 g/min
Power of laser beam	P_{laser}	1000 W
Density of liquid	ρ_l	6900 kg/m^3
Density of solid	ρ_s	7800 kg/m^3
Radius of laser beam	R	0.7 mm
Liquidus temperature	T_l	1700 K
Solidus temperature	T_s	1630 K
Melting temperature	T_m	1665 K
Dynamic Viscosity	μ_l	6×10^{-3} kg/(ms)
Velocity of laser beam	V_{laser}	12.7 mm/s
Powder velocity	V_{powder}	0.2 m/s

Figure Captions

Fig.1 Scheme of macro/micro-scale coupling method.

Fig.2 Temperature field of whole domain (powder velocity, $0.2 m/s$, powder diameter, $100\mu m$, laser beam power, 1000W, radius of laser beam, 0.7 mm, and laser absorptivity, 0.3).

Fig.3 Pure metal dendrite growth: Interface shape (contour $\phi = 0$) shown every 5000 iterations, simulation parameters, $\lambda = 6.3829$, $\alpha = 4$, $\Delta x = \Delta y = 0.4$, $\delta t = 0.008$, $\varepsilon_4 = 0.05$.

Fig.4 Convergence of dimensionless dendrite tip velocity as increasing iteration number for the simulation of pure metal dendrite growth.

Fig.5 Calculation results for alloy solidification (at dimensionless time of 52) ($MC_\infty = 0.1$, $k = 0.15$, Le = 20, D = 4.0, $\delta t = 0.0004$, $\Delta x = \Delta y = 0.4$, $\varepsilon_4 = 0.05$) (a) Phase-field distribution (b) Dimensionless composition field distribution (c) Dimensionless temperature field distribution.
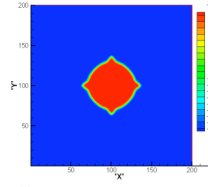
Fig.6 Scheme of cell location.

Fig.7 Microstructure evolution of cell location 1 ($MC_\infty = 0.1$, $k = 0.15$, Le = 20, D = 4.0, $\delta t = 0.0004$, $\Delta x = \Delta y = 0.4$, $\varepsilon_4 = 0.05$).

Fig.8 Microstructure evolution of cell location 2 ($MC_\infty = 0.1$, $k = 0.15$, Le = 20, D = 4.0, $\delta t = 0.0004$, $\Delta x = \Delta y = 0.4$, $\varepsilon_4 = 0.05$).

Fig.9 Microstructure evolution of cell location 3 ($MC_\infty = 0.1$, $k = 0.15$, Le = 20, D = 4.0, $\delta t = 0.0004$, $\Delta x = \Delta y = 0.4$, $\varepsilon_4 = 0.05$).

Fig.10 Effect of thermal noise strength (S) on dendrite growth pattern: (a) S=4, (b) S=10, (c) S=15, (d) S=20, and (e) S=25.
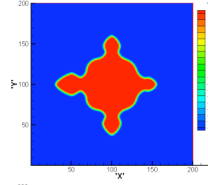
Fig.11 Effect of undercooling (Δ) on dendrite growth pattern: (a) $\Delta = 0.45$, (b) $\Delta = 0.65$, and (c) $\Delta = 0.75$
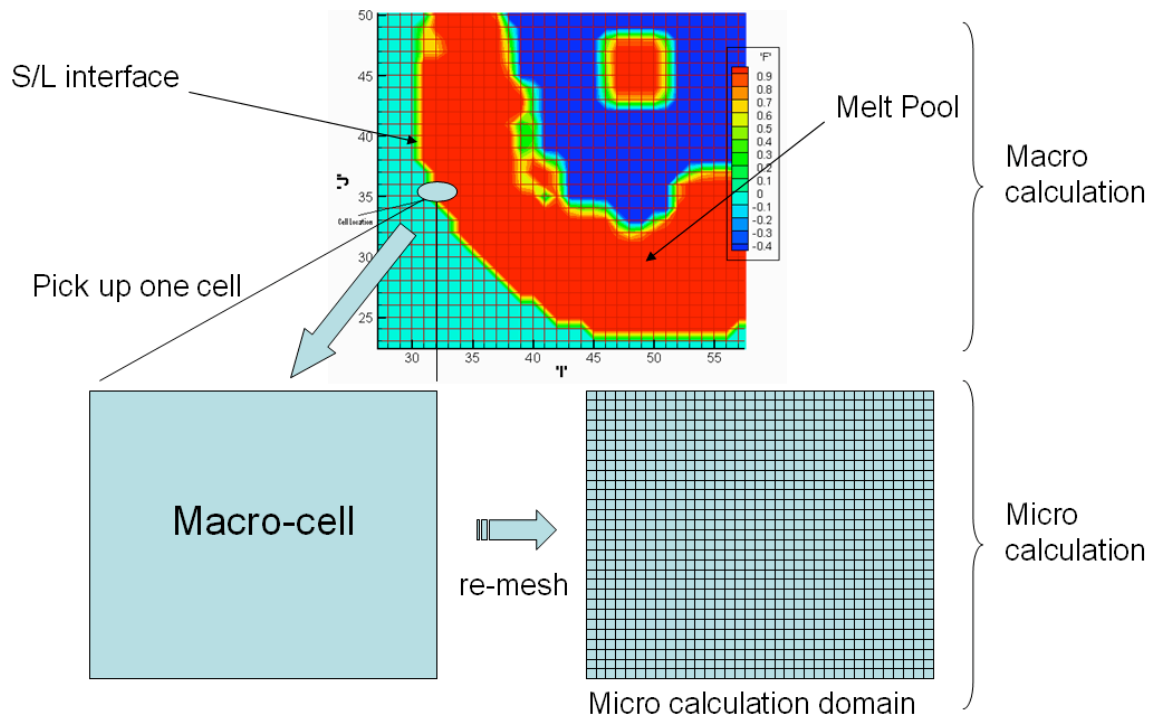
Fig.1　Scheme of macro/micro-scale coupling method
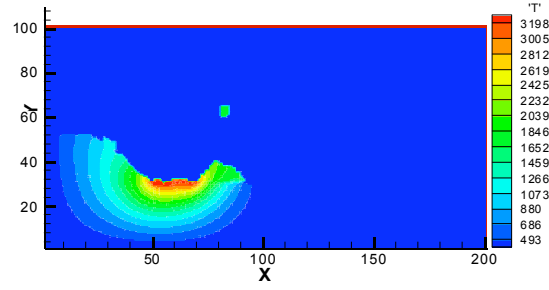
(a) t = 32 ms
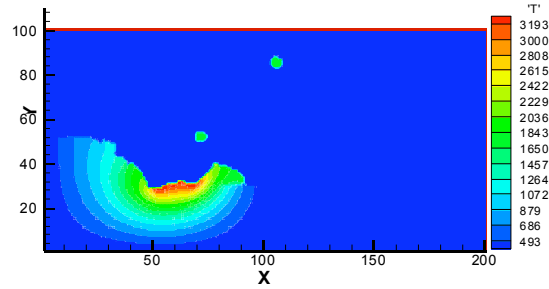
(b) t = 34 ms
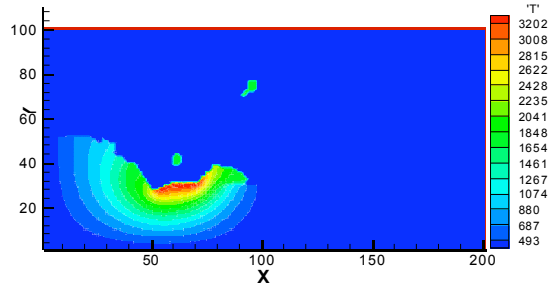
(c) t = 36 ms
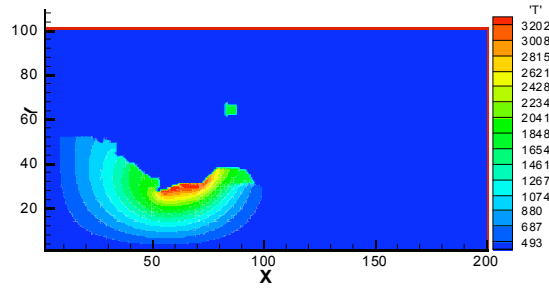
(d) t = 38 ms

Fig. 2   Temperature field of whole domain

(powder velocity, 0.2*m/s*, powder diameter, 100*μm*, laser beam power, 1000W, radius of laser

beam, 0.7 mm, and laser absorptivity, 0.3).

Fig. 3 Pure metal dendrite growth: Interface shape (contour $\phi = 0$) shown every 5000 iterations, simulation parameters, $\lambda = 6.3829$, $\alpha = 4$, $\Delta x = \Delta y = 0.4$, $\delta t = 0.008$, $\varepsilon_4 = 0.05$.

Fig. 4 Convergence of dimensionless dendrite tip velocity as increasing iteration number for the

simulation of pure metal dendrite growth

(a)
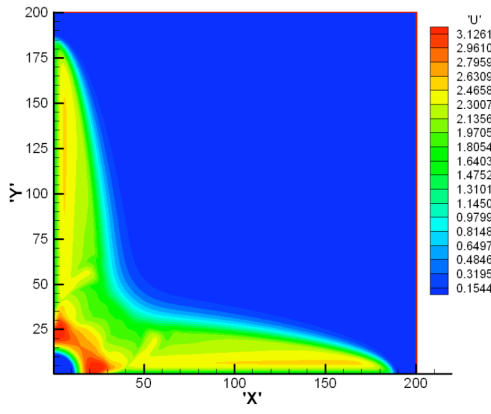
(b)
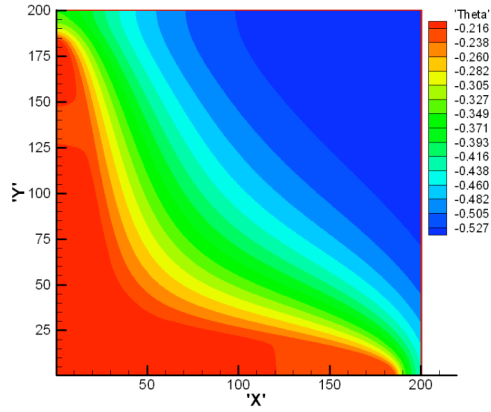
(c)

Fig. 5 Calculation results for alloy solidification (at dimensionless time of 52)
(MC_∞ = 0.1, k = 0.15, Le = 20, D = 4.0, δt = 0.0004, Δx = Δy = 0.4, ε$_4$ = 0.05)
(a) Phase-field distribution, (b) Dimensionless composition field distribution, and (c)
Dimensionless temperature field distribution

Fig.6　Scheme of cell location

Fig. 7 Microstructure evolution of cell location 1
(MC_∞ = 0.1, k = 0.15, Le = 20, D = 4.0, δt = 0.0004, Δx = Δy = 0.4, ε$_4$ = 0.05)

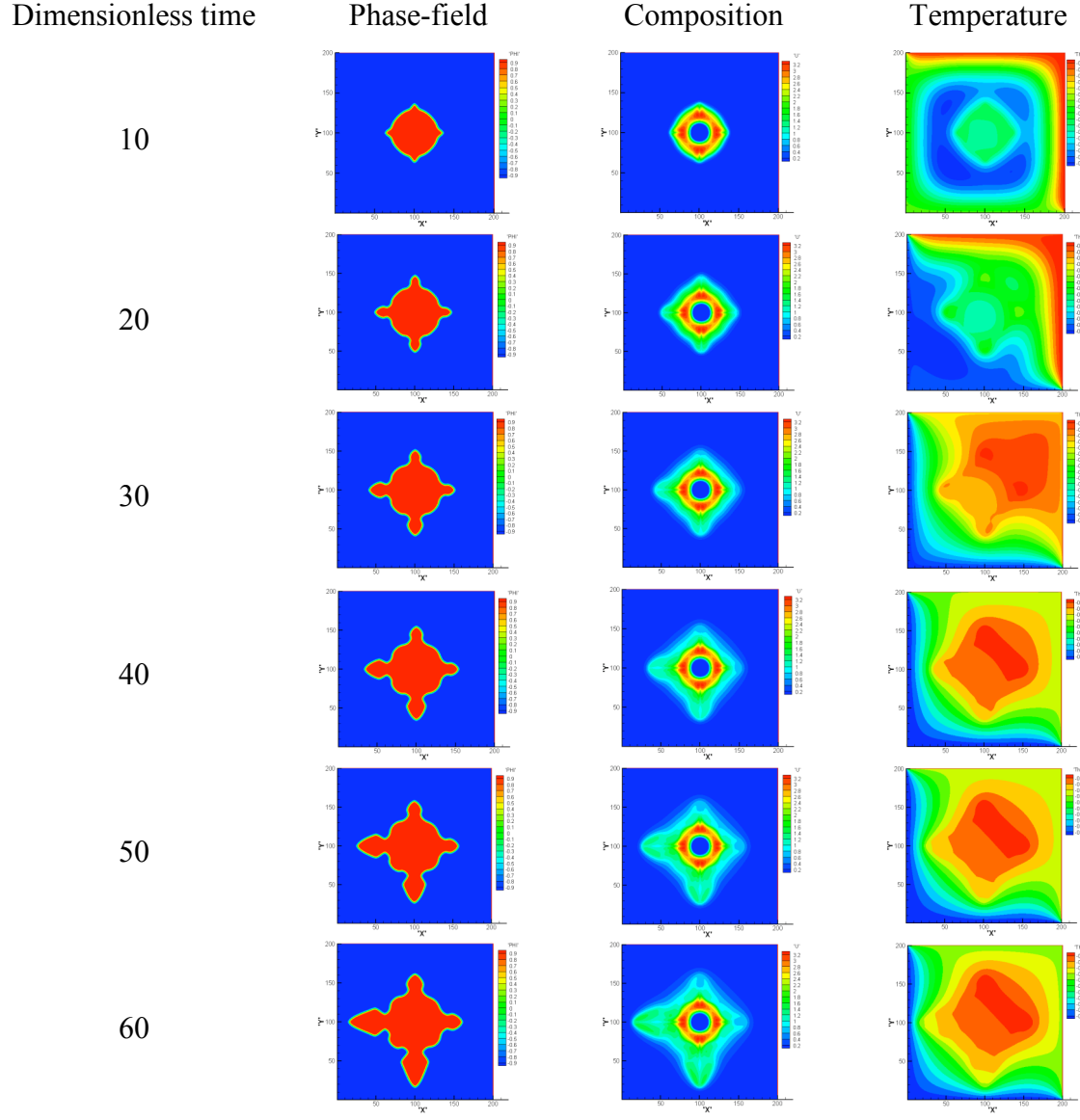Fig. 8 Microstructure evolution of cell location 2
(MC_∞ = 0.1, k = 0.15, Le = 20, D = 4.0, δt = 0.0004, Δx = Δy = 0.4, ε_4 = 0.05)

Fig. 9   Microstructure evolution of cell location 3
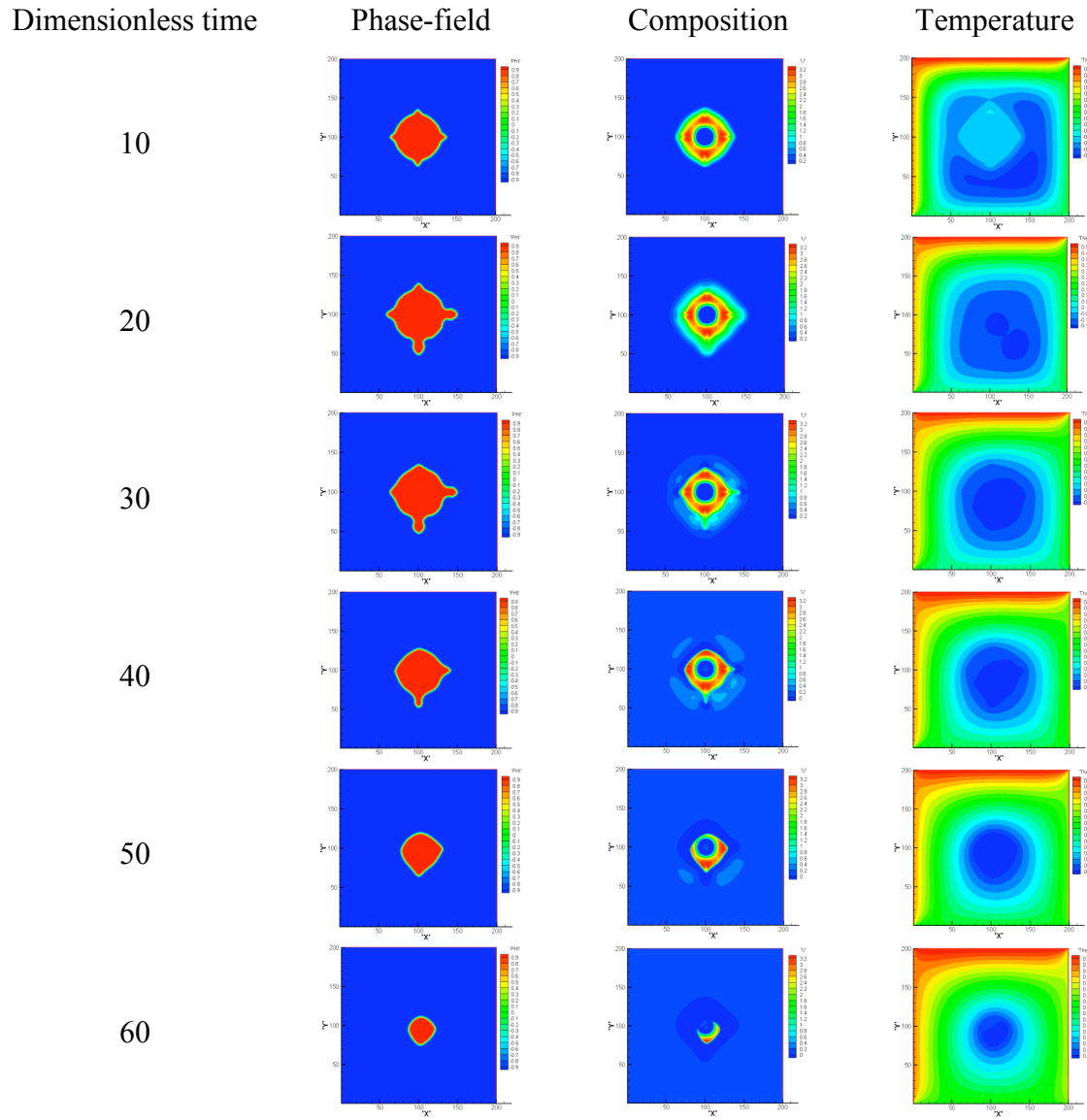(MC_∞ = 0.1, k = 0.15, Le = 20, D = 4.0, δt = 0.0004, Δx = Δy = 0.4, ε$_4$ = 0.05)

(a) S = 4

(b) S = 10

(c) S = 15

(d) S = 20

(e) S = 25

Fig. 10 Effect of thermal noise strength (S) on dendrite growth pattern
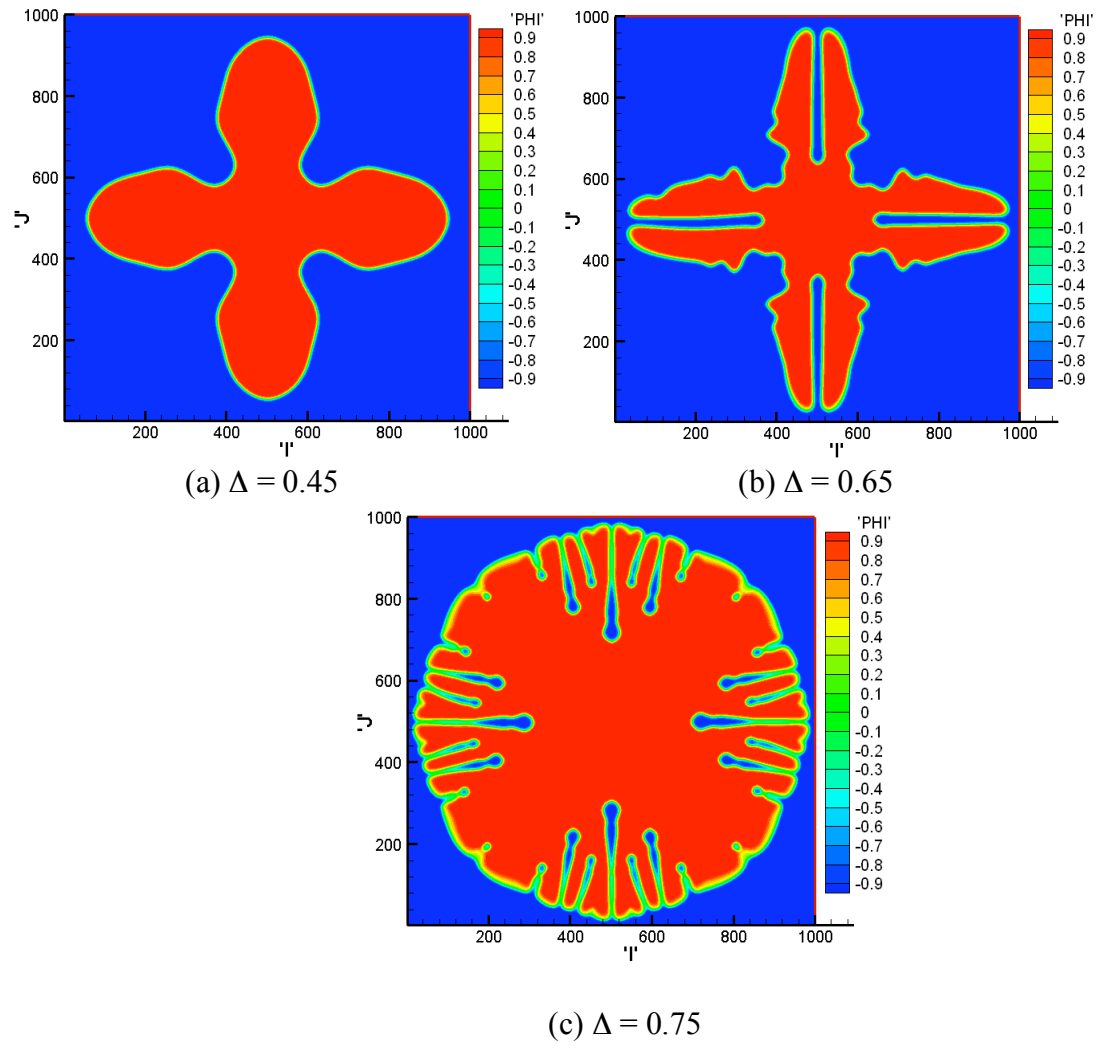
(a) Δ = 0.45

(b) Δ = 0.65

(c) Δ = 0.75

Fig. 11 Effect of undercooling (Δ) on dendrite growth pattern